Reaction of Metastable Ar*($^3P_2$) and Kr*($^3P_2$) Atoms with Water Vapor: Excitation Functions for Electronic Quenching Collisions†

Don R. Mueller and John Krenos*

Department of Chemistry and Chemical Biology, Rutgers, The State University of New Jersey, 610 Taylor Road, Piscataway, New Jersey 08854-8087

Received: February 26, 2002

In this paper, we examine the functional nature of the state-specific cross section for electronic quenching $\sigma_Q(E)$ in collisions of metastable noble gas atoms [Ar*($^3P_2$) and Kr*($^3P_2$)] with ground-state water molecules confined to a scattering-gas cell. The relative kinetic energy range studied is $E = 0.0463-0.772$ eV for Ar*($^3P_2$) and 0.0432−0.692 eV for Kr*($^3P_2$). These beam-gas-luminescence experiments incorporate a novel state-specific monitor system employing Xe gas. Photon emission from a state-specific Xe state produced in quenching collisions with the respective metastable noble gas (Ng*) atoms is a direct measure of the total disappearance of the metastable state under scrutiny in the reaction with water vapor. We use the classical orbiting and absorbing sphere models with empirically derived parameters [London dispersion C_{disp}, induction C_{ind} (spherically averaged or aligned dipole), and absorbing sphere radius r_{as}] to predict energy-dependent cross sections for the total quenching reactions. The underlying premise of the models is that although the quenching process itself is envisioned to be a short-range two-electron exchange interaction, it is the long-range attractive forces between the respective collision partners that are critical in determining whether such short-range processes ultimately occur. Values of σ_Q determined from the models are in very good agreement with our experiment. This work supersedes our previous study for Ar*($^3P_{2,0}$) [Novicki, S.; Krenos, J. *J. Chem. Phys.* **1988**, *89*, 7031].

Introduction

Quenching cross sections σ_Q for metastable noble gas atom [Ng*(^3P_J), where Ng* = Ne*($J = 2$ & 0), Ar*($J = 2$ & 0), Kr*($J = 2$ & 0), and Xe*($J = 2$)] collisions are obtained primarily from thermal (300 K) rate constant measurements k_Q in flow tube, stationary discharge, and pulse radiolysis reactors.[1] Values of σ_Q are estimated by $\sigma_Q \cong k_Q/\bar{g}$, where $\bar{g}$ is the average relative velocity of the collision partners. An advantage of this technique is that an individual metastable state Ng*($^3P_2$ or $^3P_0$) is monitored (usually by optical absorption) to yield a state-specific rate constant. The velocity dependence of σ_Q is concealed, however, by thermal averaging.

The only direct measurement of absolute, state-specific electronic quenching cross sections $\sigma_Q(g)$ was that of Gersch and Muschlitz for the reactions of Ar* and Kr* with O_2.[2] A beam-scattering-cell method, in which all the metastable atoms in the velocity-selected beam are detected on the walls of the gold-plated cell, was employed. They performed extensive measurements over a large energy range for mixed metastable beams. In a series of more difficult experiments, they used an inhomogeneous deflecting magnet to remove the $M_J = \pm 1, \pm 2$ states of Ng*($^3P_2$) from the beam, and thereby obtained a limited number of Ng*($^3P_2$) cross sections (four collision energies for Ar* and three for Kr*). With a similar apparatus, Sheldon and Muschlitz measured absolute quenching cross sections for Ar* and Kr* mixed-metastable beams ($^3P_{2,0}$) with H_2O/D_2O at a few collision energies.[3]

Using a beam-scattering-cell apparatus, we developed a monitor method for measuring $\sigma_Q(g)$ for metastable atom reactions yielding luminescent products and applied it to the reaction of Ar*($^3P_{2,0}$) with H_2O.[4] The emission intensity of OH* product observed at a fixed position in the scattering cell was plotted as a function of H_2O pressure under constant Ar* beam conditions. The total disappearance cross section Q_T of Ar* was obtained from these plots at energies between 0.048 and 0.13 eV and was attributed to the quenching reaction of Ar* by H_2O. With the assumption that $Q_Q = Q_T$, we were able to extract a deconvoluted cross section $\sigma_Q(g)$ by fitting the data to model cross section forms with adjustable parameters.[4] We recently improved our monitor method by measuring total disappearance cross sections Q_N for nonquenching collisions and found that Q_N is not negligible at lower collision energies. We devised an approximate scheme for calculating Q_Q for the Ng* + O_2 system,[5,6] where Ng = Ne, Ar, Kr, and Xe. The values of σ_Q we derived for Ar* and Kr* reactions are in excellent agreement with the results of ref 2. In this paper, we return to the Ng* + H_2O system to explore the energy dependence of quenching cross sections using a state-sensitive monitor reaction, Ng*($^3P_2$) + Xe → Ng + Xe*, where Ng = Ar and Kr. We find that the nonquenching correction has an important effect on the collision energy dependence. The results are now in harmony with the product cross section energy dependence for the reaction

$$Ar^*(^3P_{2,0}) + H_2O \rightarrow OH^*(A) + H + Ar$$

measured by Parr and Martin,[7] namely that both our absolute σ_Q values and their relative σ^*(OH*) ones have an $E^{-1/3}$ form at low collision energies.

We also test the classical orbiting and absorbing sphere models with empirically derived parameters. The orbiting model

† Part of the special issue "John C. Tully Festschrift".

10.1021/jp0205315 CCC: $22.00
Published on Web 06/28/2002

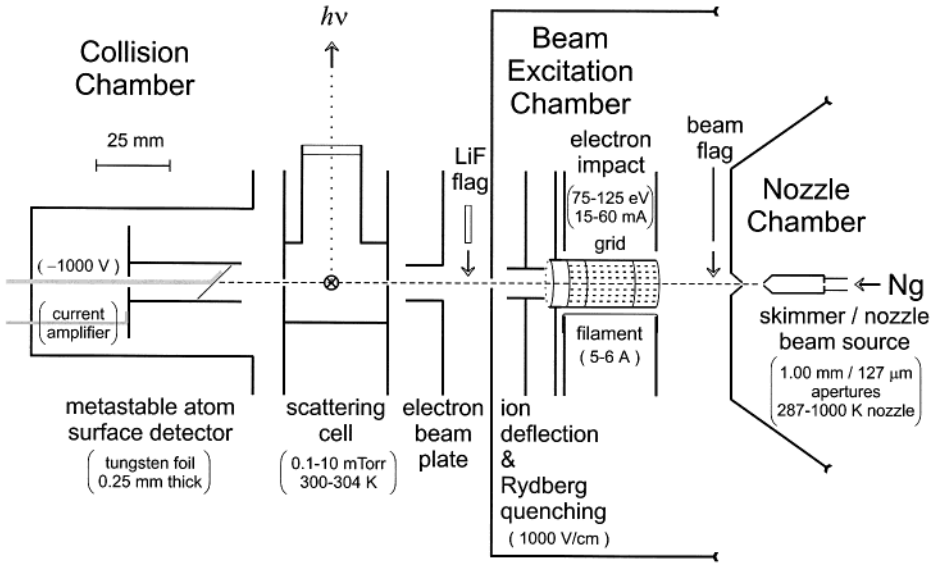

Figure 1. Schematic diagram of the molecular beam apparatus. The tungsten surface Faraday detector is shown. The channel electron multiplier (Channeltron) detector for Ng*, used for time-of-flight studies, is not shown (see Figure 2 of ref 6).

fits the data well at low collision energy, whereas the approach to absorbing sphere dependence is apparent at higher energy. The relative kinetic energy range studied is 0.0463−0.772 eV for Ar*($^3P_2$) and 0.0432−0.692 eV for Kr*($^3P_2$). As in our earlier study,[4] the predicted rate constant value at 300 K (8.1×10^{-10} cm^3 molecule^{-1} s^{-1}) is significantly larger than one determined directly (4.8×10^{-10} cm^3 molecule^{-1} s^{-1}) in a flowing afterglow apparatus for Ar*($^3P_2$) + H_2O.[8]

Apparatus and Techniques

The beam-scattering-cell apparatus (shown schematically in Figure 1) has been described previously.[4−6,9] The metastable beam of intensity I_m with root-mean-square (rms) velocity $\hat{v}_m$ is formed by transverse electron impact ($E_e = 75-150$ eV) on a supersonic noble-gas atom beam. Because we use state-specific monitor reactions, the composition of the mixed-metastable beam Ng*($^3P_{2,0}$) is not important.[10] The scattering cell is designed to allow for the mixing of two separate scattering gases prior to entry. One gas pressure can be held constant as the other is varied. The absolute pressure of a single gas or gas mixture in the cell is measured by a 0.05 mTorr resolution capacitance manometer (MKS 227A). The pressure reading is corrected for the temperature difference between the cell and the manometer diaphragm (323 K),[11] and then converted to a number density for monitor (n_M), target (n_t), or nonquenching (n_N) gas by the ideal gas relation. Light intensity $I^*_\lambda(x)$, produced along the beam path by the monitor reaction, is observed at a fixed distance ($x = 1.9 \pm 0.05$ cm) from the beam entrance aperture of the cell. The collection lens and 0.5 m monochromator are positioned to minimize the effects of viewing losses. The nominal bandwidth $\Delta\lambda$ of the monochromator (f 6.9 optics) is 4.8 nm (3 mm slit width). The GaAs phototube (RCA C31034-02) is thermoelectrically cooled (typical dark count rates are 8−15 photons s^{-1}). A single photon counting system (PARC 1110) is used to record the emission intensity. The tungsten surface−Faraday cup design is the metastable beam detector shown in Figure 1 and is generally used for single gas (nonseeded) expansions. The channeltron detector[6] is employed for higher energy seeding experiments and for time-of-flight velocity distribution measurements, $f_1(v_m)$, of the metastable atom beam. The nozzle temperature T_{noz} is varied between ambient (seasonal water cooling temperatures of 287−303 K) and 1000 K; the noble gases are seeded with H_2 to achieve the highest collision energy. The velocity distribution of Ng* is characterized by a Mach number of 18. The rms velocity of the metastable beam (unseeded) follows the perfect nozzle formula $\hat{v} = \sqrt{5kT_{noz}/m_m}$, where m_m is the mass of the beam and k is the Boltzmann constant. The average relative velocity $\bar{g}$ and relative kinetic energy $\bar{E}$ (collision energy) for beam-scattering gas collisions at beam velocity $\hat{v}_m$ and scattering cell temperature T_{SC} are determined by the method of Chantry,[12] which we extend to include averaging over the beam velocity distribution $f_1(v_m)$ in addition to the relative velocity distribution $f_2(g,T_{SC})$. A LiF beam flag, which is located near the scattering cell entrance aperture, is semitransparent to vacuum UV radiation ($\lambda > 104$ nm) and is used to determine the photon contribution to the measured beam intensity (also seen in the time-of-flight mode on the Channeltron).

In our experiments, we determine a velocity-averaged cross section Q_T for the total disappearance of metastable atoms by their interaction with the monitor Q_T^M or target Q_T^t gas. The major contribution to the value of Q_T derives from quenching collisions, but nonquenching beam losses cannot be neglected. The dominant quenching reactions are

$$Ng^* + Xe \rightarrow Ng + Xe^* \qquad (Q_Q^M, \text{ state-specific monitor quenching})$$

$$Ng^* + H_2O \rightarrow Ng + \text{products} \qquad (Q_Q^t, \text{ state-specific target quenching})$$

The nonquenching contribution Q_N is a viewing loss ascribed to large angle elastic scattering of Ng*. We developed a new technique[5,6] to determine Q_N by use of nonquenching gases (noble gases of lower atomic number than Ng*) under the same beam conditions at which Q_T is determined. To a good approximation, we obtain values of $Q_Q(\bar{g})$ by

$$Q_Q(\bar{g}) = Q_T - Q_N \qquad (1)$$

and then deduce $\sigma_Q(g)$, as will be described. A complete description of our procedure is given in ref 6.

In this study, scattering gas pressure for Xe (monitor gas) is typically set to about 2 mTorr and the variation in pressure of H_2O (target gas) used to measure Q_Q is typically 0−5 mTorr. Either He or Ne is used as the nonquencher for Ar*, whereas Ne is used for Kr*. The intensity of light measured at wavelength λ perpendicular to the beam direction at position x in the cell is given by

$$I^*_\lambda(x) = (A_\lambda S_\lambda C/A_T)\int_0^\infty\int_0^\infty \sigma^*_M(g) g n_m(x) n_M f_1(v_m) f_2(g,T_{SC})\, dg\, dv_m \quad (2)$$

where

$$n_m(x) = I_m(x)/(v_m\gamma_m) = [I_m(0)/(v_m\gamma_m)]\exp[-\sigma^M_Q(g)\,(g/v_m) n_M x] \quad (3)$$

In eq 3, the nonquenching beam loss is ignored. In addition to the symbols defined previously, A_λ is the spontaneous emission probability (s^{-1}) of a specific transition of the excited state formed directly in the monitor reaction, A_T is the sum of all A_λ for the same upper state, C is an apparatus factor (absolute photodetector response, light collection efficiency, viewing geometry, etc.), $\sigma^M_Q(g)$ is the velocity dependent quenching cross section for the monitor reaction, $n_m(x)$ is the metastable beam number density at position x in the cell, and n_M is assumed uniform throughout the cell (i.e., $n_m(x=0) \ll n_M$). If $\sigma^*_M(g)$ varies slowly with g, the exponential term in eq 3 dominates and to a good approximation

$$I^*_\lambda(x)/n_M \propto \exp[-Q^M_Q(\bar{g}) n_M x] \quad (4)$$

where

$$Q^M_Q(\bar{g}) = \int_0^\infty\int_0^\infty \sigma^M_Q(g)(g/v_m) f_1(v_m) f_2(g,T_{SC})\, dg\, dv_m \quad (5)$$

Since Q_N is nonnegligible, a log-linear plot of $I^*_\lambda(x)/n_M$ vs n_M actually yields Q^M_T according to

$$I^*_\lambda(x)/n_M \propto \exp[-Q^M_T n_M x] \quad (6)$$

where $I_m(0)$ is constant. A corrective method is then required to obtain $Q^M_Q(\bar{g})$. To estimate the nonquenching cross section Q_N, a noble gas of lower atomic number than Ng* is added to the scattering cell at a fixed monitor number density n_M. The dependence of $I^*_\lambda(x)$ on n_N is given by

$$I^*_\lambda(x) \propto \exp[-Q_N n_N x] \quad (7)$$

where $I_m(0)$ and n_M are constant. The critical assumption is that the value of Q_N obtained in this manner is identical to the nonquenching contribution for the monitor cross section as well. A value of $Q^M_Q(\bar{g})$ is then determined by eq 1. We used eq 5 to extract $\sigma^M_Q(g)$ values for Ar*($^3P_2$) + Xe and Kr*($^3P_2$) + Xe in ref 6. In this paper, the actual values of the quenching cross sections for these monitor reactions are not important. The monitor wavelength, 823.2 nm, is the same for both reactions.[6]

The above procedure is extended to measure cross sections for target gases characterized by either luminescent or "dark" quenching reactions. In a manner analogous to the nonquenching gas procedure, the target gas is added to the scattering cell at a fixed value of n_M. The dependence of $I^*_\lambda(x)$ on n_t is given by

$$I^*_\lambda(x) \propto \exp[-Q^t_T n_t x] \quad (8)$$

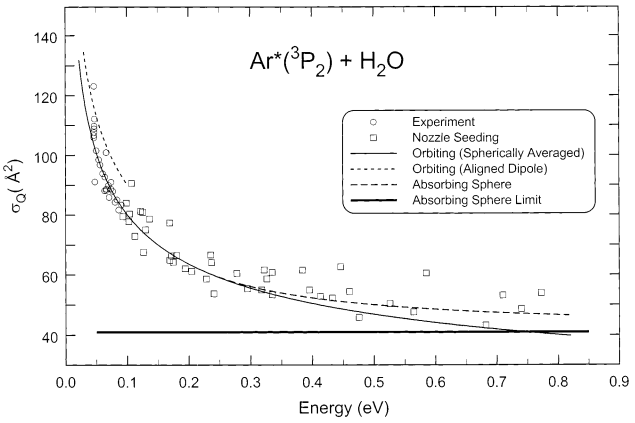

Figure 2. Electronic quenching cross sections for the Ar*($^3P_2$) + H_2O reaction. Values obtained with no nozzle seeding gas are given by open circles; nozzle seeding (H_2) results are given by open squares. The solid curve is the prediction of the spherically averaged orbiting model, the short-dashed curve (below 0.1 eV) is the prediction of the aligned dipole orbiting model, and the long-dashed curve (above 0.222 eV) is that of the absorbing sphere model. The solid straight line is the absorbing sphere limit (40.9 Å^2) at infinite collision energy.

where $I_m(0)$ and n_M are constant. A value of Q^t_T is obtained and the value of Q_N determined by the monitor reaction is used to obtain $Q^t_Q(\bar{g})$ by eq 1. In this paper, we do not deconvolute the equation

$$Q^t_Q(\bar{g}) = \int_0^\infty\int_0^\infty \sigma^t_Q(g)(g/v_m) f_1(v_m) f_2(g,T_{SC})\, dg\, dv_m \quad (9)$$

to obtain $\sigma^t_Q(g)$, rather we prefer using the method of Kinsey and co-workers[13] because of simplicity. In this treatment,

$$Q^t_Q(\bar{g}) = f(s,x)\left(\frac{\bar{g}}{\bar{v}_m}\right)\sigma^t_Q(\bar{g}) \qquad \text{and} \qquad x = v_m/v_t \quad (10)$$

where v_t is the most probable velocity of the target gas, $s = 6$ for a long-range London attractive potential, and values of $f(s,x)$ are available in tabular form.[13] As a check, we use eq 9 to predict values of $Q^t_Q(\bar{g})$ with the model cross section forms to be discussed later and agreement between experimental and predicted values is excellent.

Results

In Figure 2, we provide a plot of the electronic quenching cross sections σ_Q for the Ar*($^3P_2$) + H_2O reaction as a function of the relative collision energy $\bar{E}$ (0.0463−0.772 eV). The high and low values of σ_Q for Ar*($^3P_2$) are 123 Å^2 at 0.0466 eV and 43 Å^2 at 0.682 eV, respectively. For the Kr*($^3P_2$) + H_2O reaction, the quenching cross sections σ_Q are plotted against the relative collision energy in Figure 3 (0.0432−0.692 eV). The high and low values of σ_Q for Kr*($^3P_2$) are 127 Å^2 at 0.0440 eV and 47 Å^2 at 0.505 eV, respectively. Selected experimental values of σ_Q for Ar*($^3P_2$) and Kr*($^3P_2$) quenching reactions and those of Sheldon and Muschlitz[3] for mixed-metastable beams are given in Tables 1 and 2, respectively. Comparison between the two experimental studies is excellent. Our method for correcting the total disappearance cross section for the nonquenching beam loss is successful in this system.

The σ_Q error limits (typically ±5% for Ng*($^3P_2$) + H_2O) include both the random error obtained from the slope of plots similar to Figure 3 in ref 6 and the estimated error associated with the uncertainty in the viewing position x (±0.5 mm) and gas pressure (±0.05 mTorr). We employ nozzle seeding with

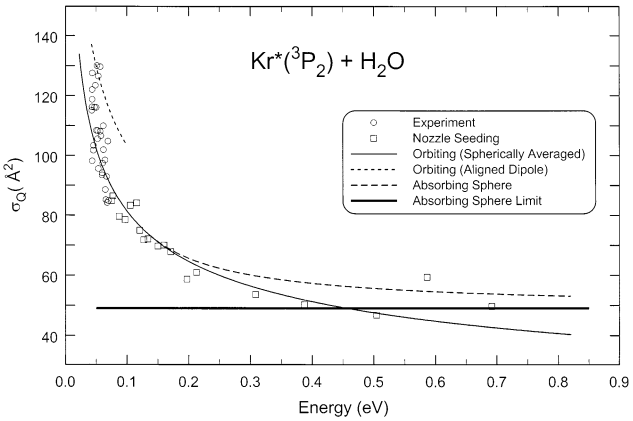

Figure 3. Electronic quenching cross sections for the Kr*($^3P_2$) + H_2O reaction. Values obtained with no nozzle seeding gas are given by open circles; nozzle seeding (H_2) results are given by open squares. The solid curve is the prediction of the spherically averaged orbiting model, the short-dashed curve (below 0.1 eV) is the prediction of the aligned dipole orbiting model, and the long-dashed curve (above 0.135 eV) is that of the absorbing sphere model. The solid straight line is the absorbing sphere limit (49.0 Å^2) at infinite collision energy.

TABLE 1: Selected Experimental Quenching Cross Sections for Ar*($^3P_2$) + H_2O[a]

Ar*	$\bar{g}$ (m/s)	$\bar{E}$ (eV)	σ_Q (Å^2)
($^3P_{2,0}$)[b]	702 (678)	0.0370 (0.0370)	107 ± 8 (110 ± 8)
($^3P_2$)	790	0.0463	106
($^3P_2$)	801	0.0476	112
($^3P_2$)	826	0.0502	102
($^3P_{2,0}$)[b]	844 (825)	0.0523 (0.0534)	99 ± 2 (98 ± 2)
($^3P_2$)	859	0.0541	98.5
($^3P_2$)	878	0.0564	96.8
($^3P_2$)	913	0.0605	93.9
($^3P_2$)	941	0.0640	92.7
($^3P_2$)	960	0.0665	88.7
($^3P_2$)	989	0.0702	89.9
($^3P_2$)	1064	0.0804	84.3
($^3P_{2,0}$)[b]	1068 (1054)	0.0808 (0.0841)	99 ± 8 (80 ± 8)
($^3P_2$)	1087	0.0837	85.1
($^3P_2$)	1188	0.0987	84.0
($^3P_2$)	1273	0.112	72.9
($^3P_2$)	1410	0.136	78.7
($^3P_2$)	1607	0.175	64.3
($^3P_2$)	2044	0.278	60.5
($^3P_2$)	2250	0.335	53.4
($^3P_2$)	2564	0.433	52.3
($^3P_2$)	2832	0.526	50.4
($^3P_2$)	3232	0.682	43.3
($^3P_2$)	3368	0.740	48.7

[a] Error ±5% (see text). See ref 9b for the complete list (70 values). [b] Reference 3. Values for Ar* + D_2O in parentheses.

hydrogen to obtain the higher relative energies (above 0.090 eV for Ar* and above 0.070 eV for Kr*). The data taken with nozzle seeding are shown in Figures 2 and 3 by open squares. The reproducibility of the values is shown clearly in the tables and figures. There is somewhat more scatter in the experimental measurements taken with nozzle seeding. For Ar*, our quenching cross section values are well within the total scattering cross sections (505 Å^2 at 708 m/s to 236 Å^2 at 4580 m/s) determined by Wang et al.[14]

Models

In our treatment, the long-range attractive potential is composed primarily of dispersive and inductive terms, both behaving as $V(r) \propto r^{-6}$. At lower collision energies, the dispersive and inductive forces acting between the collision partners should be of enhanced duration, resulting in more curved trajectories than would be possible at higher collision energies. As a consequence, we choose the orbiting model to predict the quenching cross sections at low energy. We find that the classical orbiting model, which incorporates a spherically averaged induction coefficient C_{ind} , agrees quite well with our lower energy experimental electronic quenching cross section values. For a long-range potential form, $V(r) = -C_{total}/r$,[6] the well-known close-collision orbiting cross section σ_{orb} is given by

$$\sigma_Q(E) \approx \sigma_{orb} = \left(\frac{3\pi}{2}\right)\left(\frac{2C_{total}}{E}\right)^{1/3} \qquad (11)$$

where $C_{total} = C_{disp} + C_{ind}$ (the sum of the London dispersion and induction terms).

At higher collision energies, the orbiting model should fail, at which point the repulsive part of the potential assumes greater influence on the outcome. The absorbing sphere model is adopted to predict cross section values at the higher collision energy end of our experiments. The absorbing sphere cross section is σ_{as} given by

$$\sigma_Q(E) \approx \sigma_{as} = \pi r_{as}^2\left(1 + \frac{C_{total}}{E r_{as}^6}\right) \qquad (12)$$

where r_{as} is the absorbing sphere collision distance.

We use experimental values of the fundamental electronic properties of Ng* and H_2O to calculate the model parameters C_{disp}, C_{ind}, and r_{as} rather than to fit them to our experimental results. Values of the electronic properties (mean electronic polarizability α, first ionization energy I, and electronic dipole moment μ for the ground-vibrational state) and model parameters that we have determined are given in Table 3.

The absorbing sphere radius is determined from the hard sphere model. In that model, an impact parameter b greater than the sum of the radii $r_A + r_B$ produces no collision or reaction. On the other hand, if $b \leq r_A + r_B$, a collision (in our case reaction) takes place. Hard sphere radii for Ng* and H_2O are estimated as follows. For the Ar + H_2O hard sphere collisions, Kolb et al.[23] determined a value of 1.06 Å for the radius that

TABLE 2: Selected Experimental Quenching Cross Sections for Kr* + H_2O[a]

Kr*	$\bar{g}$ (m/s)	$\bar{E}$ (eV)	σ_Q (Å^2)
($^3P_2$)	694	0.0432	115
($^3P_2$)	697	0.0437	118.7 & 98.2
($^3P_2$)	715	0.0458	103
($^3P_{2,0}$)[b]	722 (698)	0.0466 (0.0474)	112 ± 2 (119 ± 2)
($^3P_2$)	730	0.0476	116
($^3P_2$)	752	0.0504	116 & 108
($^3P_2$)	802	0.0569	130 & 108
($^3P_2$)	830	0.0606	97.4
($^3P_2$)	859	0.0646	98.4
($^3P_2$)	876	0.0671	92.9
($^3P_2$)	932	0.0751	84.9
($^3P_2$)	1010	0.0872	79.6
($^3P_2$)	1202	0.120	74.9
($^3P_2$)	1396	0.160	70.1
($^3P_2$)	1624	0.213	61.0
($^3P_2$)	1968	0.308	53.6
($^3P_2$)	2212	0.387	50.3
($^3P_2$)	2534	0.505	46.8
($^3P_2$)	2735	0.586	59.4
($^3P_2$)	2975	0.692	49.7

[a] Error ±5% (see text). See ref 9b for the complete list (51 values). [b] Reference 3. Values for Kr* + D_2O in parentheses.

TABLE 3: Parameters Used in the Orbiting and Absorbing Sphere Models

parameters	$Ar^*(^3P_2) - H_2O$	$Kr^*(^3P_2) - H_2O$
$\alpha(Ng^*)$[15]	48.4 Å^3	51.4 Å^3
$\alpha(H_2O)$[16]	1.457 Å^3	1.457 Å^3
$I(H_2O)$[17]	12.614 eV	12.614 eV
$\mu(H_2O)$[18]	1.852 D	1.852 D
$C_{disp}(Ng^*-Ng^*)$[a]	2646 eV·Å^6	2896 eV·Å^6
$C_{disp}(H_2O-H_2O)$[b]	20.17 eV·Å^6	20.17 eV·Å^6
$C_{disp}(Ng^*-H_2O)$[c]	142.6 eV·Å^6	147.4 eV·Å^6
$C_{ind}(Ng^*-H_2O)$[d]	103.4 eV·Å^6	109.8 eV·Å^6
C_{total}	246.0 eV·Å^6	257.2 eV·Å^6
r_{as}[e]	3.61 Å	3.95 Å

[a] Slater−Kirkwood method.[19] [b] London dispersion.[20] [c] Kramer Herschbach method.[21] [d] Induction − spherically averaged.[22] [e] See text (refs 23−26).

corresponds to the H_2O hard sphere derived from the average area of projection onto the collision plane of 3.52 Å^2. Assuming the same radius for H_2O in $Ng^* + H_2O$ collisions, we then need to determine r_{Ar^*} and r_{Kr^*}. We use the Bernstein−Muckerman[24] rule of thumb,

$$r_m = r_i + r_j + 2.0 \text{ Å} \tag{13}$$

for relating the radius of the potential well minimum r_m to the orbital radii of the interacting atoms r_i and r_j . For $Ar^* + Kr$, the potential minimum is located at 5.34 Å[25] and the orbital radius of Kr is 0.795 Å.[26] It follows that $r_{Ar^*} = 2.55$ Å and $r(Ar^* + H_2O) = 3.61$ Å $= r_{as}$. For $Kr^* + Ar$, the minimum is located at 5.55 Å[25] and the orbital radius of Ar is 0.659 Å.[26] Therefore, $r_{Kr^*} = 2.89$ Å and $r(Kr^* + H_2O) = 3.95$ Å $= r_{as}$. In the absorbing sphere model, attractive interactions can bend the trajectory to within the critical distance for reaction, r_{as}. At a given energy, there is a maximum impact parameter for which this occurs. At sufficiently high energy, $b_{max} \approx r_{as}$. The predicted high energy limiting cross sections are then 40.9 Å^2 and 49.0 Å^2 for Ar* and Kr*, respectively.

Discussion

As seen in Figures 2 and 3, the orbiting model with spherically averaged induction fits the data well. There is a slight deviation (underestimation) at low energy for $Ar^* + H_2O$ and a somewhat larger one for Kr*. The lower energy deviation may represent collisions in which induction is enhanced by dipole alignment. The leveling off at high energies (approach to πr_{as}^2) is fairly well described by the absorbing sphere model for $Ar^* + H_2O$, but the effect is less clear for Kr*. More experimental data are needed in this case. It may be that our value of r_{as} is overestimated for Kr*.

The inclusion of induction in the model is important. By excluding the spherically averaged induction term,[22]

$$C_{ind} = \overline{\frac{1}{2}(3\cos^2\theta + 1)}\alpha_{Ng^*}\mu_{H_2O}{}^2 = \alpha_{Ng^*}\mu_{H_2O}{}^2 \qquad \left[\text{Note: } \overline{\cos^2\theta} = \frac{1}{3}\right] \tag{14}$$

we find that model cross sections are 20% smaller for both Ar* and Kr*. In the aligned dipole model ($\theta = 0°$ or 180°), the value of C_{ind} doubles. Our dispersion term with spherically averaged induction provides the best agreement with experiment except at the very lowest energies, at which point values given by the aligned dipole model represent an upper bound. Quantum calculations performed by Bentley[27] for Ne^*-H_2O predict that the most favorable approach of Ne* on the potential energy surface is toward the O atom end of the H_2O molecule in C_{2v} symmetry with a well depth of about 0.25 eV.

We have now established that the quenching cross section has the same energy dependence $E^{-1/3}$ as the luminescent cross section ($Ar^* + H_2O \rightarrow Ar + OH^* + H$) measured by Parr and Martin[7] (0.025−0.13 eV). Parr and Martin also observed a change in energy dependence (positive deviation) at their higher energies (0.13−0.89 eV) and also a positive deviation from the orbiting energy form at the lowest energies. The branching fraction σ^*/σ_Q we measure at 0.047 eV is 0.24 ± 0.05,[6] a value in good agreement with one obtained in a discharge flow system.[28] The higher energy luminescent cross sections of Tabayashi and Shobatake[29] (0.3−1.8 eV) clearly display the weak energy dependence as well. The branching fraction may well be energy independent. If it is, their experimental luminescent cross section range of 8−10 Å^2 translates into limiting quenching cross section values of 33−42 Å^2, a range that encompasses our model value of 40.9 Å^2. We attribute the different energy dependence in our earlier study[4] to the neglect of the nonquenching contribution to Q_T, which is more important at lower collision energies.

We have also studied the analogous $Ng^*(^3P_0) + H_2O$ quenching reactions and find a comparable falloff behavior in the cross sections, the main difference is that the magnitudes are roughly 20−25% smaller.[9b,30] This is unusual in that for most reactions of Ng*, the $^3P_0$ level is more easily quenched.[1]

The orbiting model parameters are related to the quenching rate constant k_Q by

$$k_Q(T) = \frac{3}{2}\sqrt{\frac{2^3\pi}{\mu}}(2C_{total})^{1/3}(kT)^{1/6}(0.902745) \tag{15}$$

where μ is the reduced mass (not the dipole moment) and k is the Boltzmann constant. For $T = 300$ K, the predicted rate constants are 8.1×10^{-10} cm^3·mol^{-1}·s^{-1} for $Ar^* + H_2O$ and 7.5×10^{-10} cm^3·mol^{-1}·s^{-1} for $Kr^* + H_2O$. The value for Ar* is considerably larger than the experimental one,[8] 4.8×10^{-10} cm^3·mol^{-1}·s^{-1}. The reason for this difference is unclear. The model only yields this value of the rate constant at $T = 12.8$ K, an unphysical result.

Conclusions

We have explored the energy dependence of the quenching cross section for the $Ng^* + H_2O$ system using a state-sensitive monitor reaction, $Ng^*(^3P_2) + Xe \rightarrow Ng + Xe^*$, where Ng = Ar and Kr. We find that the nonquenching correction has an important effect on the collision energy dependence. The quenching results are now in accord with the product cross section ($Ar^* + H_2O \rightarrow OH^* + H + Ar$) energy dependence measured by Parr and Martin,[7] namely, that both our absolute σ_Q values and their relative $\sigma^*(OH^*)$ ones follow an $E^{-1/3}$ form at low collision energies.

We have also tested the classical orbiting and absorbing sphere models with empirically derived parameters. The orbiting model fits the data well at low collision energy, whereas the approach to the absorbing sphere dependence is apparent at higher energy, which is seen most clearly for Ar* quenching. As in our earlier study,[4] the predicted rate constant value at 300 K is significantly larger than one determined directly in a flowing afterglow apparatus for $Ar^*(^3P_2) + H_2O$.[8]

Acknowledgment. Financial support from the Research Council, Computing Services, and Department of Chemistry and Chemical Biology of Rutgers, The State University, is gratefully

acknowledged. Our work has benefited from correspondence and/or conversations with Professors M. F. Golde, H. Haberland, K. A. Hardy, H. Hotop, E. E. Muschlitz, Jr., D. W. Setser, P. E. Siska, J. W. Sheldon, and A. J. Yencha. We are deeply indebted to B. Van Assen for many seminal discussions about intermolecular forces and for essential encouragement. Finally, we wish to recognize the early support, guidance, and friendship of Professors R. Wolfgang, Z. Herman, D. R. Herschbach, and J. C. Tully, who we are privileged to honor on this festive occasion.

References and Notes

(1) (a) Brom, J. M., Jr.; Kolts, J. H.; Setser, D. W. *Chem. Phys. Lett.* **1977**, *55*, 44. (b) Yokoyama, A.; Hatano, Y. *Chem. Phys.* **1981**, *63*, 59. (c) Velazco, J. E.; Kolts, J. H.; Setser, D. W. *J. Chem. Phys.* **1978**, *69*, 4357. (d) Sobczynski, R.; Setser, D. W. *J. Chem. Phys.* **1991**, *95*, 3310. (e) The Xe($^3P_0$) atoms have been produced in a flow tube reactor, and emission spectra from excited reaction products were reported [Zhong, D.; Setser, D. W. *Chem. Phys. Lett.* **1993**, *207*, 555].

(2) Gersch, M. E.; Muschlitz, E. E., Jr. *J. Chem. Phys.* **1973**, *59*, 3538.

(3) Sheldon, J. W.; Muschlitz, E. E., Jr. *J. Chem. Phys.* **1978**, *68*, 5288.

(4) Novicki, S.; Krenos, J. *J. Chem. Phys.* **1988**, *89*, 7031. [Note that the value of parameter *A* in model I is 9.68×10^{-10} in the units given, but the σ_Q values determined by the model and reported in the paper are correct.]

(5) Mueller, D.; Krenos, J. *J. Phys. Chem.* **1993**, *97*, 2106.

(6) Rickey, D.; Krenos, J. *J. Chem. Phys.* **1997**, *106*, 3135.

(7) Parr, T. P.; Martin, R. M. *J. Phys. Chem.* **1978**, *82*, 2226.

(8) De Jong, H. J. *Chem. Phys. Lett.* **1974**, *25*, 129.

(9) (a) BelBruno, J. J. Ph.D. Thesis, Rutgers, The State University, 1980. (b) Mueller, D. R. Ph.D. Thesis, Rutgers, The State University, 2000.

(10) Beam composition studies using monitor reactions will be reported by us in *Rev. Sci. Instrum*. The details of this method, which requires the measurement of both the intensity of a spectral feature linked to Ng*($^3P_2$) and the intensity of the mixed-state beam as function of electron impact voltage, will be described.

(11) Loriot, G.; Moran, T. *Rev. Sci. Instrum.* **1975**, *46*, 140.

(12) Chantry, P. J. *J. Chem. Phys.* **1971**, *55*, 2746.

(13) Lang, N. C.; Lilenfeld, H. V.; Kinsey, J. *J. Chem. Phys.* **1971**, *55*, 3114.

(14) Wang, K.; Li, J.; Hardy, K. A.; Sheldon, J. W. *Phys. Rev. A* **1994**, *49*, 2630.

(15) Miller, T. M.; Bederson, B. *Adv. At. Mol. Phys.* **1977**, *13*, 1.

(16) Russell. A. J.; Spackman, M. A. *Mol. Phys.* **1995**, *84*, 1239.

(17) Brehm, B. *Z. Naturforsch.* **1966**, *21a*, 196.

(18) Shostak, S. L.; Ebenstein, W. L.; Muenter, J. S. *J. Chem. Phys.* **1991**, *94*, 5875.

(19) Slater, J. C.; Kirkwood, J. G. *Phys. Rev.* **1937**, *37*, 682.

(20) (a) London, F. *Z. Phys. Chem. Abt. B* **1930**, *11*, 222. (b) London, F. *Z. Phys.* **1930**, *63*, 245.

(21) Kramer, H. L.; Herschbach, D. R. *J. Chem. Phys.* **1970**, *53*, 2792.

(22) Hirschfelder, J. O.; Curtiss, C. F.; Bird, R. B. *Molecular Theory of Gases and Liquids*; John Wiley: New York, 1964.

(23) Kolb, C. E.; Baum, H. R.; Tait, K. S. *J. Chem. Phys.* **1972**, *57*, 3409.

(24) Bernstein, R. B.; Muckerman, J. T. *Adv. Chem. Phys.* **1967**, *12*, 389.

(25) Kerstel, E. R. T.; Van Kruysdijk, C. P. J. W.; Vlugter, J. C.; Beijerinck, H. C. W. *Chem. Phys.* **1988**, *121*, 211.

(26) Waber, J. T.; Cromer, D. T. *J. Chem. Phys.* **1965**, *42*, 4116.

(27) Bentley, J. *J. Chem Phys.* **1980**, *73*, 1805.

(28) Balamuta, J.; Golde, M. F. *J. Chem. Phys.* **1982**, *76*, 2430.

(29) Tabayashi, K.; Shobatake, K. *J. Chem. Phys.* **1988**, *88*, 835.

(30) D. Mueller and J. Krenos, to be published.